Review of Scientific Instruments

An innovative Yb-based ultrafast deep ultraviolet source for time-resolved photoemission experiments

Cite as: Rev. Sci. Instrum. **85**, 123903 (2014); https://doi.org/10.1063/1.4903347
Submitted: 12 September 2014 . Accepted: 22 November 2014 . Published Online: 10 December 2014

F. Boschini, H. Hedayat, C. Dallera, P. Farinello, C. Manzoni, A. Magrez, H. Berger, G. Cerullo, and E. Carpene

An innovative Yb-based ultrafast deep ultraviolet source for time-resolved photoemission experiments

F. Boschini,[1] H. Hedayat,[1] C. Dallera,[1] P. Farinello,[2] C. Manzoni,[3] A. Magrez,[4] H. Berger,[4] G. Cerullo,[1] and E. Carpene[3,a)]
[1]*Dipartimento di Fisica, Politecnico di Milano, 20133 Milan, Italy*
[2]*Dipartimento di Ingegneria Industriale e dell'Informazione, Università di Pavia, 27100 Pavia, Italy*
[3]*IFN-CNR Dipartimento di Fisica, Politecnico di Milano, 20133 Milan, Italy*
[4]*Institute of Condensed Matter Physics (ICMP), École Polytechnique Fédérale de Lausanne (EPFL), CH-1015 Lausanne, Switzerland*

(Received 12 September 2014; accepted 22 November 2014; published online 10 December 2014)

Time- and angle-resolved photoemission spectroscopy is a powerful technique to study ultrafast electronic dynamics in solids. Here, an innovative optical setup based on a 100-kHz Yb laser source is presented. Exploiting non-collinear optical parametric amplification and sum-frequency generation, ultrashort pump ($h\nu = 1.82$ eV) and ultraviolet probe ($h\nu = 6.05$ eV) pulses are generated. Overall temporal and instrumental energy resolutions of, respectively, 85 fs and 50 meV are obtained. Time- and angle-resolved measurements on BiTeI semiconductor are presented to show the capabilities of the setup. © *2014 AIP Publishing LLC*. [http://dx.doi.org/10.1063/1.4903347]

I. INTRODUCTION

The combination of ultrafast laser spectroscopy with angle-resolved photoemission spectroscopy (ARPES) offers a unique opportunity for direct time-domain studies of electron dynamics in solids. Time- and angle-resolved photoemission spectroscopy (TR-ARPES) is a technique in which a femtosecond laser pulse (the pump) perturbs the electronic population of a system and subsequently an ultraviolet probe pulse with photon energy larger than its work function (usually 4–5 eV) ejects photoelectrons with a specific direction and energy. By changing the delay between pump and probe pulses one can monitor different elementary processes associated with ultrafast relaxation of the pump-perturbed electronic distribution. During the last decade, TR-ARPES has been extensively employed to investigate various materials such as metals,[1–4] cuprates,[5–8] and topological insulators.[9–12] An alternative time-resolved photoemission technique is two-photon photoemission spectroscopy (2PPE), in which a combination of pump and probe pulses, each of which has not enough energy to overcome the material work function, is used for photoemission. 2PPE allows probing ultrafast temporal evolution of occupied and unoccupied states.[13–16]

Differently from 2PPE, TR-ARPES directly provides a snapshot of the electronic energy dispersion and allows a temporal reconstruction of photoinduced modifications of the electronic bands of the system in the reciprocal space. This technique has particularly evolved owing to developments in ultrafast laser technology. The characteristics of the driving laser influence the main experimental parameters, e.g., pulse energy, time resolution, and acquisition time. In low frequency sources (typically working at 1-kHz repetition rate), space-charge effect[17] and low signal-to-noise ratio are the main problems. Space-charge effect, a result of Coulomb repulsion among emitted photoelectrons, broadens and shifts the photoelectron spectra.[18,19] To avoid such effect, the probe fluence must be kept low enough so that one or at most a few photoelectrons per pulse are emitted; hence, in order to achieve a high signal-to-noise ratio, it is necessary to average over a large number of laser shots. For 1-kHz systems, the acquisition times become impractically long; for this reason TR-ARPES is typically performed at 100-250 kHz repetition rates. The light source traditionally employed for the generation of pump and probe pulses is a cw-pumped, regeneratively amplified Ti:sapphire laser, operating at a repetition rate $\geq$100 kHz.[20] The pump pulses are a fraction of the laser fundamental frequency (FF) at 1.55 eV (800 nm wavelength), while 6.2-eV (200-nm) probe pulses are obtained by fourth harmonic generation.[21–24] Usually low-repetition rate sources supply pulses with mJ-level energy, which can drive high-harmonic generation of probe pulses with photon energies of the order of several tens of electronvolts, allowing versatile valence and core photoemission setups in spite of a lower generation efficiency in comparison with second order nonlinear processes and typically longer acquisition times.[25–28]

Recently, Yb-doped gain media have emerged as promising materials for femtosecond laser sources. Both in bulk and fiber formats they have several advantages such as long excited state lifetimes, allowing direct diode pumping and easy scaling to high repetition rates, and low quantum defect, allowing the efficient extraction of high average powers with low thermal loads, also leading to excellent stability. For these reasons, Yb-based regeneratively amplified femtosecond laser systems are nowadays emerging as an alternative technology to Ti:sapphire lasers. However, despite these promising characteristics, no TR-ARPES system driven by an Yb laser has been reported so far. Table I summarizes the main features of our Yb-based light source, which will be outlined in details in Sec. II A, and compares them with two state-of-the-art Ti:sapphire-based systems (Refs. 22 and 23) taken as indicative examples.

a)ettore.carpene@polimi.it

TABLE I. Comparison of performances between our Yb-based setup and two Ti:sapphire-based setups.

	Repetition rate	Pump pulse energy	Pump pulse tunability	Energy resolution (meV)	Temporal resolution (fs)
Boschini *et al.*	10–350 kHz	0.45 μJ (100 kHz)	1.45–2 eV	53	85
Smallwood *et al.*[22]	1 kHz–54 MHz	<10 nJ (500 kHz)	1.48 eV (oscillator 1.25–1.75 eV)	23	300
Faure *et al.*[23]	250 kHz	3 μJ	1.5–1.6 eV	70	65

In this paper, we describe a novel TR-ARPES setup based on a high-repetition rate Yb laser exploiting nonlinear optical processes in order to generate ultrashort visible pump pulses (30 fs-1.82 eV) and deep ultraviolet (DUV) pulses (80 fs-6.05 eV) with high tunability. The high repetition rate (100 kHz) and the good stability of all optical processes permit to achieve a large signal-to-noise ratio and a reduced acquisition time without the influence of space-charge effects. Detection of photoemitted electrons is performed by a time-of-flight (TOF) energy analyzer, an alternative to hemispherical energy analyzers typically used in TR-ARPES experiments.

The paper is organized as follows: in Sec. II, we describe in detail the experimental apparatus used for the generation of pump and probe pulses and the experimental setup used for TR-ARPES. In Sec. III, we present experimental TR-ARPES results on BiTeI sample to assess the performance of the new setup.

II. EXPERIMENTAL SETUP

Section II will describe in detail the innovative optical setup and the achieved performances of the TR-ARPES apparatus. The ultra-high vacuum (UHV) system, the TOF spectrometer, and the data acquisition system have been already discussed in a previous paper[21] in which a 1 kHz TR-ARPES system is presented in detail. The system has been optimized for efficient operation at 100 kHz repetition rate.

A. Optical setup

The experimental setup starts with a regeneratively amplified Yb:KGW system (Pharos, Light Conversion) producing 6-W (pulse energy stability <0.5% rms/24 h), 290-fs pulses at 1028 nm, with repetition rate set at 100 kHz. Yb-based femtosecond laser systems present many advantages in terms of compactness, wall-plug efficiency, long-term reliability, and average power. However, if compared with Ti:sapphire lasers, they cannot be directly applied to TR-ARPES for the following reasons: (i) their pulse duration is typically of the order of 200-400 fs, therefore the temporal resolution is lower than sub-100-fs Ti:sapphire lasers; (ii) their photon energy is only 1.2 eV thus the generation of 6-eV pulses requires higher order nonlinear processes than starting from 1.6-eV Ti:sapphire pulses. To overcome these limitations, we developed a dedicated system based on optical parametric amplification and frequency conversion. The source delivers pulses with energy of 60 μJ, high enough to initiate the cascade of nonlinear processes necessary for the generation of the ultrashort DUV pulses for photoemission experiments.[29,30] Although a complex optical system is necessary to prepare the pulses for TR-ARPES measurements, the high output pulse energy and the generally lower cost and maintenance time of Yb-based laser sources in comparison with high-repetition rate regeneratively amplified Ti:sapphire lasers suggest that the first are promising sources in new TR-ARPES setups. The energy per pulse, higher than the usual amount supplied by Ti:sapphire lasers, allows the generation of high-intensity energy-tunable sub-100-fs pulses by means of nonlinear optical processes, giving access to unexplored pump-energy dependent excitation effects.

Schematically (see Fig. 1), the system starts with a broadband non-collinear optical parametric amplifier (NOPA) delivering pulses at 680 nm (1.82 eV), with spectra supporting 15-fs transform-limited (TL) duration. A fraction of this light is directly used as a pump for the TR-ARPES experiment: the remaining pulse energy contributes to the generation of the DUV probe. To this aim, the visible pulses are frequency doubled to generate 340-nm (3.65 eV) light and then mixed with the second harmonic (SH, 2.4 eV) of the laser source by sum-frequency generation (SFG), thus generating DUV pulses at 205 nm (6.05 eV), with spectra corresponding to 65-fs TL pulse length.

The layout of the NOPA is detailed in Fig. 2. The s-polarized FF beam is first split by a 90% transmission (T)/10% reflectance (R) beamsplitter (BS1). The weak reflected beam (1.5 μJ energy) is focused with a 50-mm focal-length lens into a 6-mm thick undoped YAG plate to generate a white-light supercontinuum (WLC).[31] In the spectral range of interest (630–740 nm), the WLC has rms energy fluctuations lower than 1%. The residual FF is filtered out from the WLC by using two broadband dielectric mirrors with high-reflectivity in the 630–740 nm spectral range and high transmittivity around 1030 nm. The remaining 90% FF light transmitted by BS1 is subsequently split to supply both the NOPA and the SFG stage. The light transmitted by beamsplitter BS2 has energy of 40 μJ and is frequency doubled in a

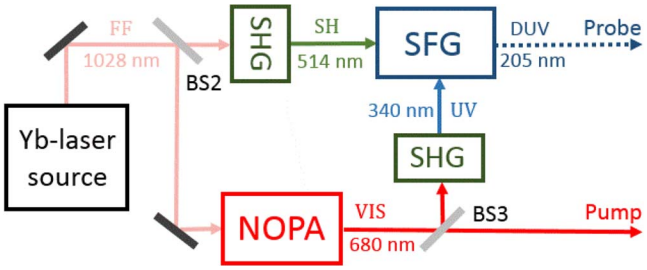

FIG. 1. Scheme of the optical modules for the generation of pump and probe pulses. FF: fundamental frequency, SH: second harmonic, UV: ultraviolet, DUV: deep ultraviolet; SHG: second harmonic generation stage, NOPA: non-collinear parametric amplifier, SFG: sum-frequency generation stage, BS: beam-splitter.

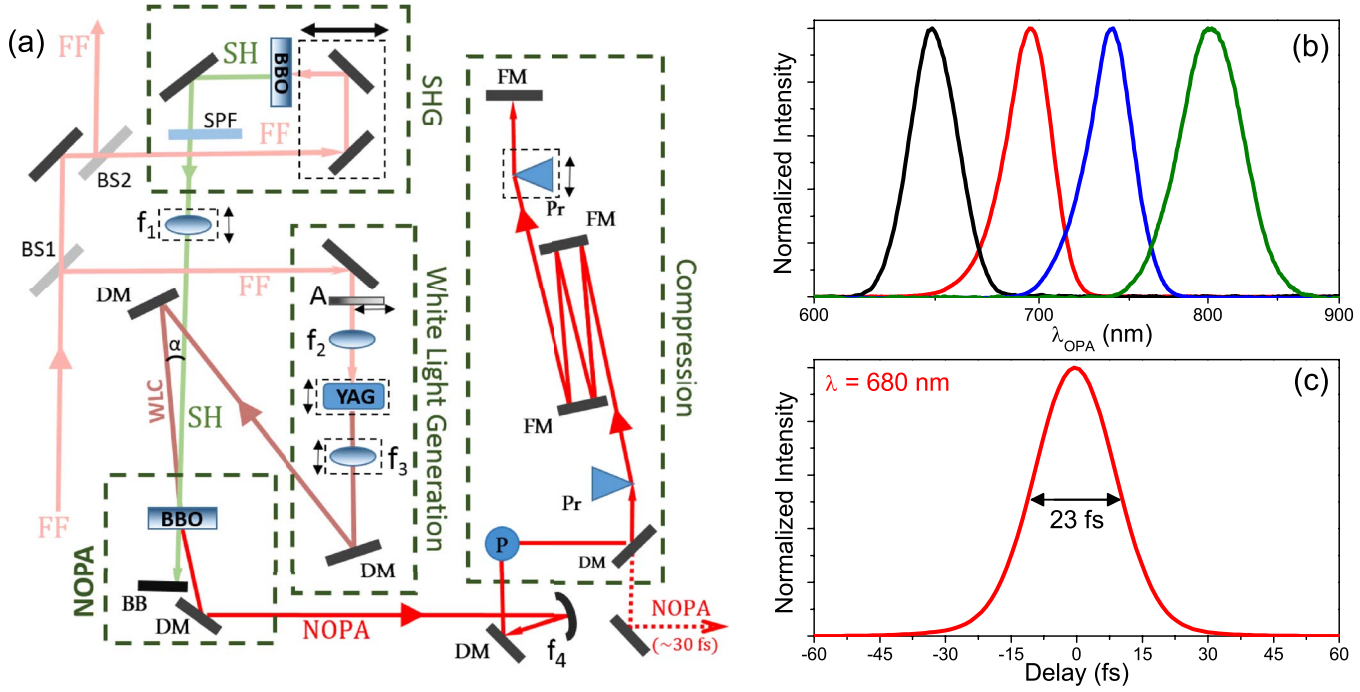

FIG. 2. (a) Scheme of the NOPA system. WLC = white-light continuum seed; BS: beam-splitter, SPF: short-pass filter, DM: dichroic/dielectric mirror, A: variable attenuator, BB = beam-blocker, P = periscope, Pr = fused silica prism, FM = folding and steering mirrors added for compactness of the compressor. $f_1 = 300$ mm, $f_2 = 50$ mm, $f_3 = 30$ mm, and $f_4 = 250$ mm. (b) Tunability of the NOPA system between 620 and 850 nm. (c) 23-fs intensity profile retrieved from FROG measurements of the compressed NOPA beam tuned at 680 nm.

3-mm thick Type-I β-barium-borate (BBO) crystal, cut at 23.4°; the process generates 15 μJ SH pulses (37% conversion efficiency), used to pump the NOPA. The residual FF is removed by a dichroic mirror and a short-pass filter (BG 39); the SH pump and WLC seed are focused in a 2-mm thick Type-I BBO crystal (22°) by, respectively, a 300-mm focal-length lens and a thin 30-mm focal-length lens, to minimize temporal dispersion of WLC colors. Pump and signal interact in the nonlinear crystal in a non-collinear configuration, leading to broadband phase-matching condition.[32–34] The internal angle between pump and seed is $\alpha \approx 1.8°$ in order to maximize the phase-matching bandwidth around 680 nm. At pump peak intensity of ≈ 40 GW/cm^2, the amplified-pulse energy is 1.3 μJ. A delay line in the optical path of the SH pump beam allows to adjust the temporal overlap between the pump and a spectral fraction of the chirped WLC. In Fig. 2(b), we show a sequence of normalized NOPA output spectra which support TL pulse duration of ≈15 fs. Due to the dispersion of the seed, the effective pulse duration is of the order of 240 fs, as obtained from frequency-resolved optical gating (FROG) measurements.

A prism-pair compressor system (equipped with Brewster angle fused silica prisms, 81.5 cm distance between the apexes of prisms) compresses the pulse down to 23 fs, as deduced from FROG measurements. Figure 2(c) reports the retrieved intensity of the pulse envelope: the intensity has a good Gaussian shape and no pre- and post-pulses are observed. A periscope rotates the polarization of the NOPA output from s to p to minimize reflection losses at the prisms' surfaces: the throughput of the compressor is further enhanced by employing folding and steering mirrors with low group-delay dispersion and high-reflectivity (630–740 nm working bandwidth). The output beam energy of the compressed pulse is 1.1 μJ, corresponding to overall 15% losses.

The compressed amplified NOPA beam is split by a 1 mm dielectric 20% T/80% R beam-splitter (BS3). The reflected 0.85-μJ fraction acts as the pump beam for TR-ARPES experiments. In order to preserve the pump pulse intensity and its duration up to the sample, we only used low group-delay dispersion, high-reflectivity Ag-coated multilayer mirrors, optimized for both s and p polarizations. This allows pumping the sample with the same fluence at any light polarization. After all reflections, a pump energy of 0.45 μJ reaches the vacuum chamber.

The 0.2-μJ signal beam transmitted by BS3 is focused onto a Type-I BBO crystal (35°). The crystal has a thickness of 150 μm, and generates SH light around 340 nm (ultraviolet, UV), with bandwidth supporting 30-fs TL pulse.

Finally, SFG between the 340-nm UV pulses and the 514-nm SH pulses generates DUV light centered at 205 nm; a scheme of the SFG setup is shown in Fig. 3. The FF 10-μJ light transmitted by the 80% T/20% R BS2 is frequency doubled in a 2.5-mm thick Type-I, 23.4°-cut BBO crystal. A telescope reduces the FF beam size to enhance the conversion efficiency leading to a pulse energy of the SH of 0.8 μJ. A zero-order half-wave plate rotates the polarization of the SH beam to fulfill the Type-I phase-matching condition for the final SFG stage. This stage employs a 50-μm BBO crystal, cut at 80°; the crystal thickness ensures an up-conversion bandwidth corresponding to a 65-fs TL pulse (see inset Fig. 3). The SH and UV beams are focused in the crystal by a 50-mm focal length Ag concave mirror. The beams are

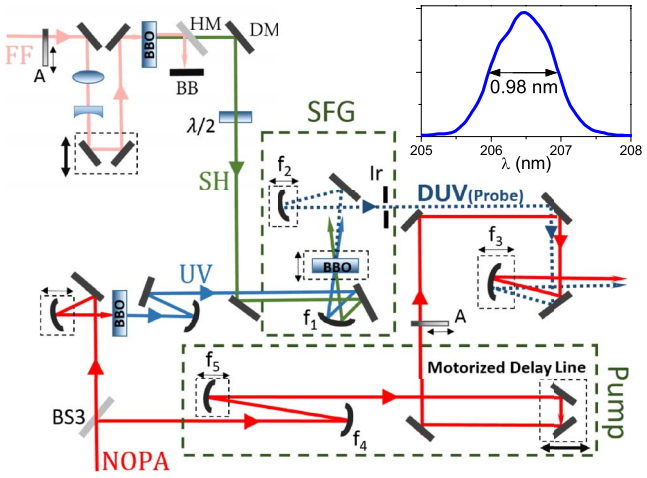

FIG. 3. Scheme of the SFG system. UV: ultraviolet, NOPA second harmonic (340 nm), DUV: deep ultraviolet, obtained by frequency mixing between SH and UV (205 nm); A: variable attenuator, HM: hot mirror, BB: beam-blocker, DM = dichroic mirror, λ/2: zero-order half-wave plate, BS: beam-splitter, Ir: iris. $f_1 = 50$ mm, $f_2 = 250$ mm, $f_3 = 500$ mm, f_4-f_5: 3:2 telescope. The inset shows the DUV spectrum: 0.98-nm bandwidth supports a 65-fs TL duration.

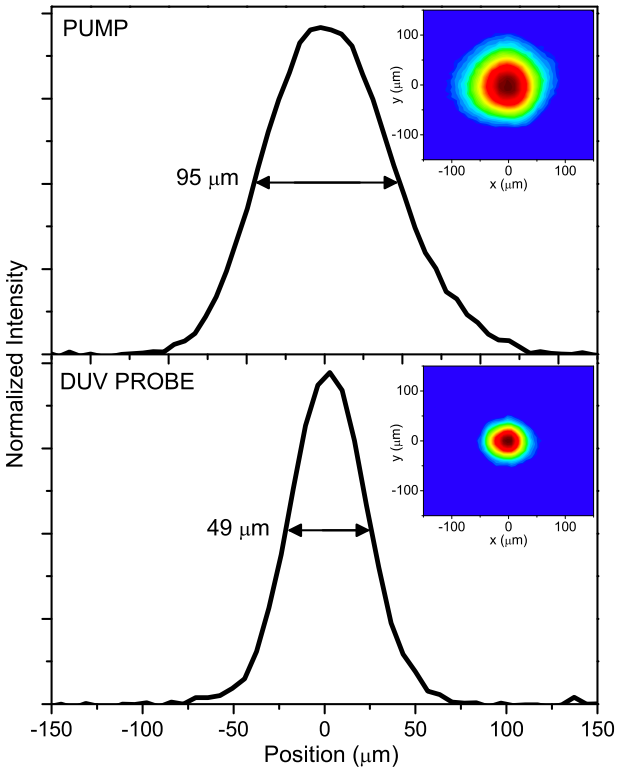

FIG. 4. Pump and DUV probe beam profiles at the sample. The measured beam profiles are shown in the insets; the main panels provide cuts along the diameter.

arranged in a non-collinear configuration (angle of 7°) to allow the separation of the broadband DUV light from the input beams; the resulting angular dispersion of the DUV beam is negligible and it does not affect TR-ARPES experiments. After collimation, the beam is steered towards the UHV chamber by low-loss UV-enhanced Al mirrors.

B. TR-ARPES setup

The standard TR-ARPES experiment consists of (i) exciting the sample with an intense pump pulse to bring the electronic population of the system to a non-equilibrium condition, and (ii) tracking the evolution of the electronic population by a probe pulse. The pump optical-path can be changed by a motorized delay stage to vary the temporal pump-probe delay with steps of 3.33 fs, well below the temporal resolution imposed by the pulses' cross-correlation. A temporally delayed probe DUV pulse photoemits electrons from the sample directly revealing the ultrafast photoinduced dynamics of electrons around the Fermi level (E_F). The specimen is kept in a vacuum chamber with base pressure of 10^{-10} mbar (UHV), required to detect photoemitted electrons, to preserve the sample surface quality and, as a consequence, to minimize multi-photon absorption effects, a critical requirement for TR-ARPES experiments.[35]

The visible pump and the DUV probe described in Sec. II A are focused on the sample inside the UHV chamber by means of a 500-mm focal-length UV-enhanced aluminum concave mirror, which avoids temporal broadening and chromatic aberrations. The incidence angle of the DUV beam on the sample is 45°. Pump and probe spatial overlap in the focus is first visually checked by means of a phosphor-coated target placed in the vacuum chamber, in the same focal plane of the sample. The entrance window of the vacuum chamber is a 2-mm-thick MgF_2 plate, which has a high transmission (>98%) for the pump wavelength. MgF_2 has low dispersion from visible to DUV spectral range: we estimate that the window stretches the ≈1-nm-broad DUV to 76-fs duration, and the visible to less than 30 fs.

In order to optimize both the pumping and the TR-ARPES pump-probe signal, pump and probe pulses should fulfill two important requirements at the interaction point on the surface of the sample: (i) the pump fluence must usually range from tens of μJ/cm^2 to some mJ/cm^2 depending on studied sample (from semiconductors to metals); (ii) the DUV pulse needs to probe all the excited area, hence its spot-size in the focus has to be smaller than that of the pump one. To achieve such conditions, we enlarged the pump and DUV spot-sizes by means of 3:2 ($f_4 - f_5$) and 5:1 ($f_1 - f_2$) telescopes, respectively; this configuration allows to obtain 100-μm-wide pump and 50-μm-wide probe beams, as shown by intensity profiles reported in Fig. 4.

The temporal resolution of the setup can be directly extrapolated by TR-ARPES measurements, as suggested by Smallwood *et al.*[22] with a noble metal as Au, and by Mauchain *et al.*[36] with BiTeI, a semiconductor material with giant Rashba splitting. Following this approach, as we will detail in Sec. III B, we could deduce a pump-probe cross-correlation (instrumental response function, IRF) of about 85 fs FWHM, mainly limited by the DUV pulse duration. Pre-compensation of the DUV pulse could lead to a duration closer to its TL at the sample surface, hence improving the experimental temporal resolution.

Photoemitted electrons are detected by means of a TOF spectrometer which measures the time required by photoexcited electrons to fly a fixed path; from this measurement, it is

possible to deduce their kinetic energy. The drift tube of the analyzer is composed by three electrodes whose biases can be independently adjusted in order to compensate contact potentials or to act as electrostatic focusing system. At the end of the TOF drift length a 16-independent-channels microchannel plate (MCP) in chevron configuration is placed. The size of the detector and the drift length guarantee an acceptance angle around 3.2° with no applied voltages to the TOF drift tube and to the sample. This angle can be reduced to 1.6° by selecting only the four central channels of the MCP, increasing the angular sensitivity for ARPES experiments. A more comprehensive description of the analyzer can be found in our previous paper.[21] ARPES maps are recorded by rotating the sample normal with respect to the TOF analyzer axis.

In ARPES measurements, the number of photoemitted electrons per pulse has to be controlled to avoid space-charge effect. Thus, the intensity of the DUV probe pulse can be adjusted by modifying the intensity of the SH beam driving the SFG process. Also the intensity of the pump has to be controlled by a variable attenuator, in order to avoid multi-photon excitations.

III. EXPERIMENTAL RESULTS

To test the performances of the developed TR-ARPES setup, we studied BiTeI, a polar layered semiconductor where stacking order of Bi, Te, and I layers breaks the inversion symmetry of the system. The lack of inversion symmetry, the large spin-orbit interaction, and the small bulk energy gap (around 400 meV) induce a giant Rashba splitting of conduction and valence bands away from the center of the surface projected Brillouin zone.[37] Consequence of a strong band bending is the Fermi level crossing of the bulk conduction band and the appearance of surface states.[36,38]

The sample is cleaved *in situ*. The occurrence of stacking faults results in Te- or I-terminated surface domains with a typical size of 150 μm.[38] Different domains show a different surface band structure allowing the identification of the surface elements directly from ARPES measurements.

We present here both static ARPES and TR-ARPES experiments on BiTeI, putting particular emphasis on space-charge effect. Moreover, we evaluate the temporal and energy resolution of the setup.

A. BiTeI: ARPES

Due to its complex energy band structure, fast electronic response and slow electronic relaxation processes, BiTeI is a benchmark sample to check the performance of the experimental apparatus. In addition, the 50-μm DUV spot-size allows to probe a single species-terminated domain of the surface. Figure 5 presents a static ARPES measurement. The probed surface reciprocal-space wave-vector is related to the kinetic energy E_k of the photoexcited electron and to its angle of emission θ with respect to the normal of the sample by the simple relation $k_{||} = \sqrt{2m_e E_k}\sin\theta/\hbar$, where m_e is the effective mass of the electron and $\hbar$ is the reduced Planck constant. Usual work functions of materials are around 4–5 eV, thus a

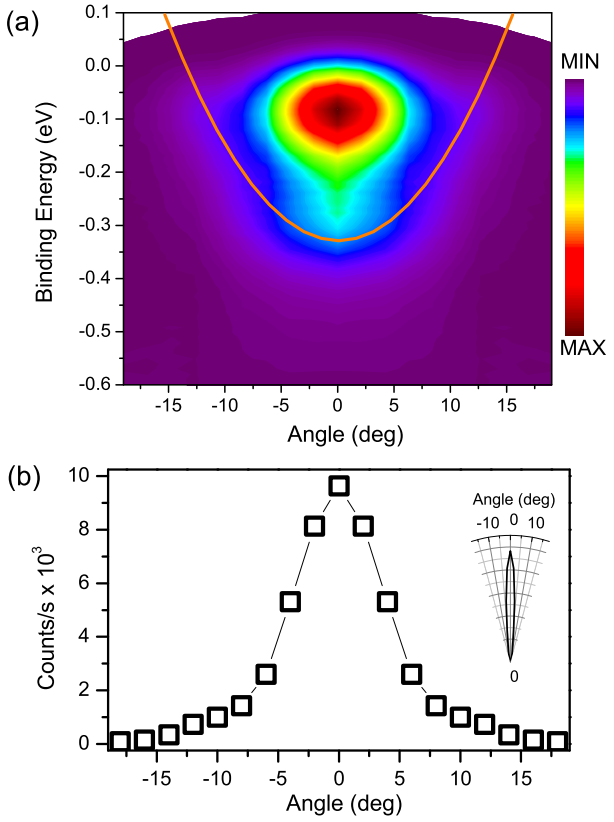

FIG. 5. (a) Static ARPES intensity map of BiTeI as the function of the binding energy and the emission angle at 80 K. The solid line is a guide to the eye for the parabolic dispersion. (b) The rate of counts as the function of the emission angle. The inset shows the rate of counts in polar coordinates revealing a restricted cone of emission from the sample.

photon energy of 6 eV permits to probe only a reduced area of the projected surface Brillouin zone (± 0.2 Å^{-1}).

In measurements presented here, both the sample and the TOF spectrometer are biased at -5 V in order to avoid effects of stray fields leading to a reduction of the acceptance angle. We enabled only the four central channels of the MCP to achieve better angular resolution.

Figure 5(a) shows the ARPES intensity map at 80 K as a function of the emission angle and the binding energy. The results are similar to those reported by Mauchain *et al.*[36] suggesting that the probed spot is a Te-terminated domain. Figure 5(b) shows the count rate as the function of the detection angle, indicating a restricted emission cone from the sample, as evidenced by the inset. DUV pulses at 6 eV are more sensitive to bulk states than to surface states and consequently the surface contribution is small. As a consequence of this bulk sensitivity, the well-known k-split parabolic surface states[37–39] cannot be observed and only a positive parabolic bulk dispersion is evidenced in Fig. 5(a). Bulk bands are Rashba split[39] (0.05 Å^{-1} shift of parabolic dispersive states from the center of the Brillouin zone) but their splitting cannot be resolved due to the lack of resolving power on wave-vectors normal to the surface.

The typical count rate for electrons emitted perpendicularly to the surface is 10 000/s, corresponding to 0.1 electron/pulse at 100 kHz repetition rate. Figure 6(a) shows space-

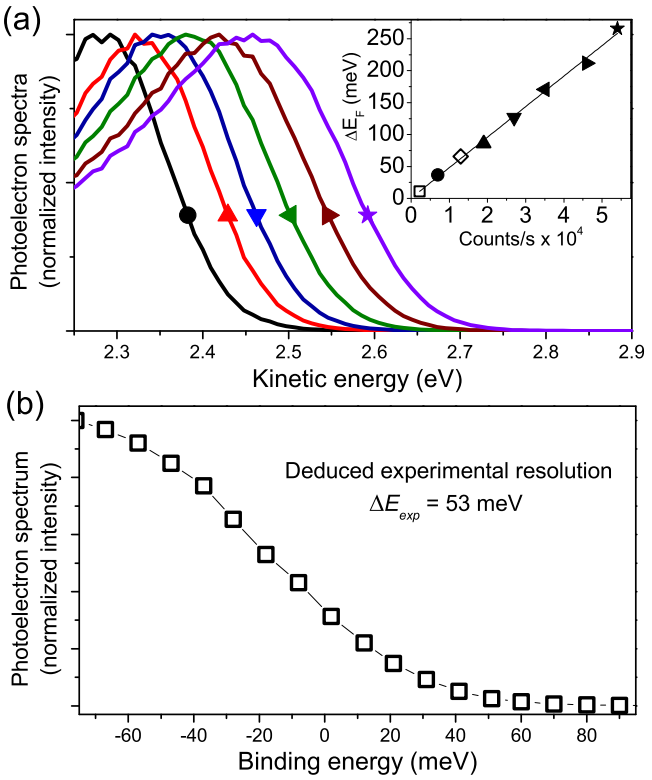

FIG. 6. (a) Space-charge effect on the Fermi edge as the function of the number of detected electrons. The inset shows the linear dependence of the space-charge induced energy shift from E_F on the count rate. (b) Fermi edge at 80 K for $k_{||} = 0$ Å^{-1}.

charge effects as the function of the rate of counts for $k_{||} = 0$ Å^{-1} . The inset of Fig. 6(a) shows the linear dependence between the Fermi edge drift and the rate of counts. As it will be shown in the following, the chosen photoemission rate shifts E_F of 50 meV due to space-charge effects, which is comparable to the energy resolution of our analyzer. This provides an optimum compromise between integration time and space-charge-induced broadening.

Figure 6(b) shows the Fermi edge measured at normal emission and at 80 K. It is well known that the electronic distribution is governed by the Fermi Dirac (FD) distribution across E_F with a width of some k_BT, where T is the temperature of the electronic system. A fit of the Fermi edge with a FD function permits the extraction of the experimental energy resolution.[21] From the fit a resolution-related effective temperature $T_e = \sqrt{T^2 + (\frac{\Delta E_{exp}}{4k_B})^2}$ can be found, where ΔE_{exp} is the related instrumental energy resolution. Knowing the system is kept at $T = 80$ K, $\Delta E_{exp} = 53$ meV instrumental energy resolution can be retrieved. The kinetic energy of electrons emitted close to E_F is around 2.3 eV. The energy resolution of the TOF related to uncertainties of the time of flight and the drift length can be estimated around 10 meV for kinetic energies of 2 eV.[21] Operating with ultrashort pulses a further energy broadening has to be taken into account: a 65-fs TL Gaussian pulse is associated to an energy uncertainty of 28 meV. The combined ΔE_{exp} deriving from the two contributions should therefore be ≈ 30 meV. The overall experimental resolution turns out to be worse possibly due to other contributions such as space-charge effect, electronic jitter, and stray fields. Compensating the work-function difference between the sample and the TOF (applying a positive potential to the sample) can push experimental resolution down to 40 meV.

B. BiTel: TR-ARPES

The system, kept at 80 K, is optically pumped with 1.82 eV pulses at a fluence of 250 μJ/cm^2. Due to the negligible momentum carried by pump photons, photoinduced transitions are vertical in the reduced k-space. Figure 7(a) shows spectra measured at different delays for emission normal to the sample ($k_{||} = 0$ Å^{-1}). The related electronic temperature after 300 fs is ≈ 800 K. Photoemission spectra are acquired at several pump-probe delays. In order to reduce the effects due to slow fluctuations of the laser source, at every pump-probe delay each spectrum is integrated over many laser shots, and the full delay scan is then repeated and averaged until the resulting trace has sufficient statistical quality. A typical acquisition scheme consists of 12 cycles of 5-s acquisition for each pump-probe delay. At 300 fs pump-probe delay we observe a clear excitation above the Fermi edge. In the center of the projected Brillouin zone, the depletion of electrons below E_F is larger than the number of the excited electrons above E_F, suggesting a directional photoexcitation of electrons away from the center of the probed k-space. All spectra are normalized to the amplitude of the peak 0.1 eV below E_F before the pump arrival in order to highlight relative k-dependence of transient excitation effects. Photoinduced effects can be finely extrapolated by computing the difference between spectra after the pump excitation and unperturbed ones. Figure 7(b) is the difference intensity map at 300 fs pump-probe delay as a function of energy and emission angle. A depletion is clearly visible for negative binding energies and excited electrons follow a parabolic dispersion above E_F, in agreement with the dispersion of Fig. 5(a). A stronger depletion is detected 0.1 eV below E_F for $k_{||} = 0$ Å^{-1} in correspondence of the crossing of the two bulk Rashba split parabolic states (± 0.05 Å^{-1}).[36] The ultrafast angle-resolved dynamics of hot electrons is more visible using logarithmic intensity maps (Fig. 7(c)) where a more efficient relative excitation at the edges of the probed k-space is detected. This effect is ascribable to the presence of a higher number of empty states for larger $k_{||}$ in association with bulk positive parabolic dispersive states crossing the Fermi edge. The difference map at 50 fs shows how, after the photoexcitation, non-thermal electrons are efficiently photoexcited at the edges of the probed k-space area of the conduction band and how they subsequently decay towards the center of the projected reciprocal-space in some picoseconds.

The temporal resolution of the optical setup is retrieved directly from TR-ARPES measurements. A photoemission angle of 8° is set in order to see the highly efficiently photoexcited electrons. The pump fluence is increased up to 400 μJ/cm^2 to fill empty states well above E_F. In Fig. 8, spectra at different delays are shown. At 30 fs and 100 fs delays, the excited electronic population is not thermalized yet (i.e.,

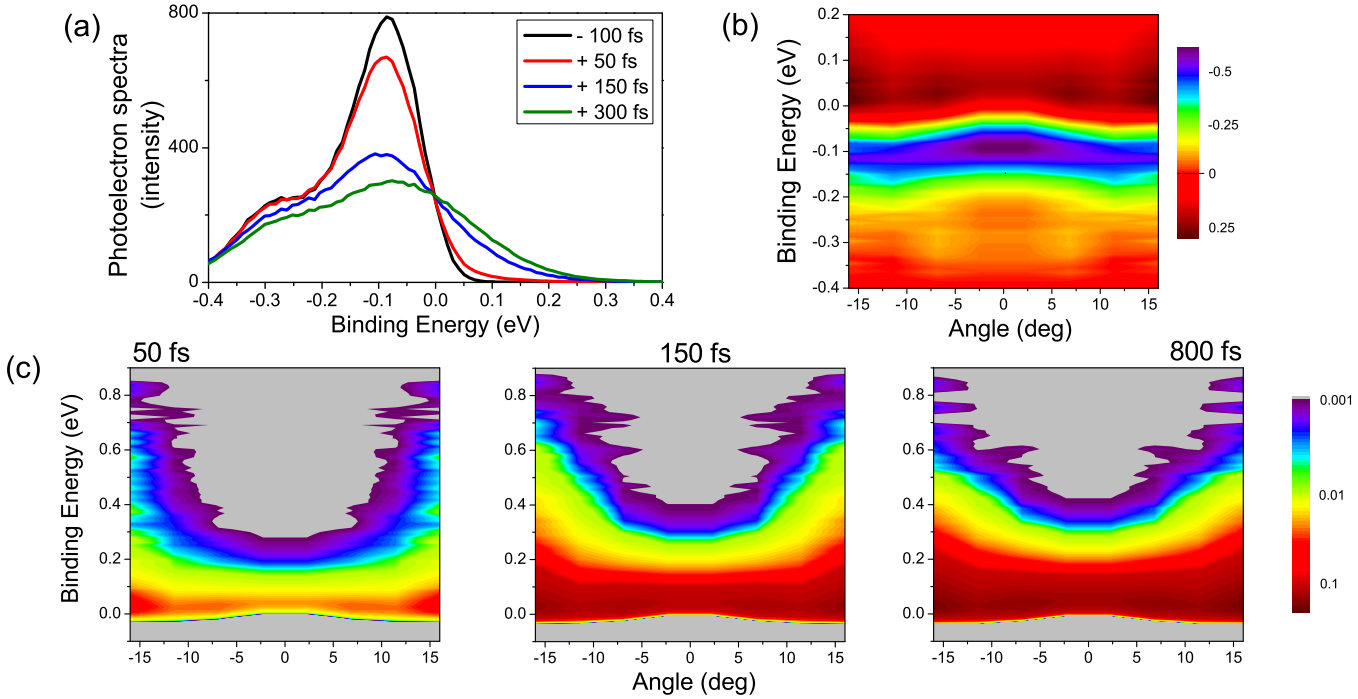

FIG. 7. TR-ARPES measurements on BiTeI at 80 K, pump fluence 250 μJ/cm^2. (a) Measured spectra at $k_{||} = 0$ Å^{-1} for different pump-probe delays; a clear photoinduced depletion/population below/above E_F is observed. (b) Linear normalized difference map as the function of the binding energy and the emission angle at 300 fs pump-probe delay; an intense depletion is present in the center of the k-space and a parabolic dispersive hot carriers excitation is observed. (c) Log normalized difference maps as the function of the binding energy and the emission angle for 50, 150, and 800 fs pump-probe delays; a relatively efficient parabolic excitation at edges of the probed k-space followed by a slow decay towards the center of the Brillouin zone is highlighted.

it does not follow a FD distribution). This means that the temporal resolution of our setup, determined by the pump-probe cross-correlation, is high enough to follow the thermalization process of the excited photoelectrons. Probing at energies 1 eV above E_F, hot electrons decay on a shorter time scale with respect to those at lower energies in agreement with Fermi liquid theory[40] where the decay time of an electron with energy E is proportional to $(E - E_F)^{-2}$. In the inset of Fig. 8, we plot the rise time of counts related to detected electrons in the energy region 0.9–1.1 eV above E_F. This energy window was chosen because it is the highest energy level reached by the photoexcited electrons and therefore the displayed time decay is not altered by contributions from electrons with higher energy. The fast rise time is followed by a decay of the signal. In order to extract the IRF corresponding to the width of the cross-correlation between pump and DUV pulses, raw data are fitted by the convolution between Gaussian and exponential decay functions. The decay time of hot electrons is ≈515 fs and the FWHM of the cross-correlation is ≈85 fs. Since the pump pulse is shorter than 30 fs, the cross-correlation duration is mainly determined by the DUV pulse (≈80 fs), in good agreement with estimation discussed in Sec. II.

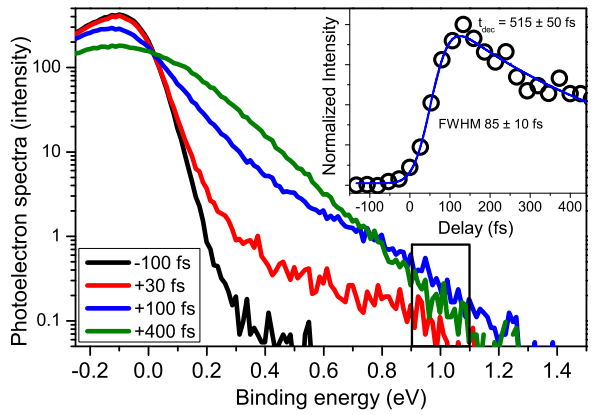

FIG. 8. (a) Photoelectron spectra as the function of the binding energy for different pump-probe delays, pump fluence 400 μJ/cm^2, for 8° emission angle. The inset shows the rise time of the number of counts is the 0.9–1.1 eV energy region: a fit with the convolution between Gaussian and exponential decay functions allows the extrapolation of a pump-probe cross-correlation time of ≈ 85 fs and an electronic decay time of ≈515 fs.

IV. CONCLUSIONS

In this paper, we described a novel 100 kHz Yb-based TR-ARPES setup. A cascade of nonlinear processes provides DUV pulses to perform high signal-to-noise TR-ARPES measurements. A NOPA system ensures a wide pump and probe wavelength tunability and the generation of 23-fs and 65-fs nearly TL pump and DUV pulses, respectively. Photoemitted electrons are detected by means of a TOF analyzer. The temporal and energy resolution of the system is 85 fs and 50 meV, respectively. Spot-sizes are carefully adjusted to work with a ratio of 2 between pump and probe beam diameters to optimize the photoemission signal. A compromise between statistical quality and acquisition time for measured spectra and experimental results, in good agreement to previously investigations,[36] guarantees optimum working conditions of our apparatus. The energy of our Yb:KGW system is suffi-

cient to drive a second independent NOPA for the generation of tunable pump pulses. This upgrade will allow the user to tune probe and pump photon energies independently, ensuring a uniquely tunable TR-ARPES setup.

ACKNOWLEDGMENTS

Fondazione Cariplo is gratefully acknowledged for financial support. G.C. acknowledges support by the EC under Graphene Flagship (Contract No. CNECT-ICT-604391). C.M. acknowledges support by the MIUR FIRB Grant No. RBFR12SW0J.

[1]G. Ferrini, F. Banfi, C. Giannetti, and F. Parmigiani, Nucl. Instrum. Methods Phys. Res. A **601**, 123 (2009), special issue in honour of Professor Kai Siegbahn.
[2]W. S. Fann, R. Storz, H. W. K. Tom, and J. Bokor, Phys. Rev. Lett. **68**, 2834 (1992).
[3]H.-S. Rhie, H. A. Dürr, and W. Eberhardt, Phys. Rev. Lett. **90**, 247201 (2003).
[4]A. Weber, F. Pressacco, S. Günther, E. Mancini, P. M. Oppeneer, and C. H. Back, Phys. Rev. B **84**, 132412 (2011).
[5]L. Perfetti, P. A. Loukakos, M. Lisowski, U. Bovensiepen, H. Eisaki, and M. Wolf, Phys. Rev. Lett. **99**, 197001 (2007).
[6]R. Cortés, L. Rettig, Y. Yoshida, H. Eisaki, M. Wolf, and U. Bovensiepen, Phys. Rev. Lett. **107**, 097002 (2011).
[7]J. D. Rameau, S. Freutel, L. Rettig, I. Avigo, M. Ligges, Y. Yoshida, H. Eisaki, J. Schneeloch, R. D. Zhong, Z. J. Xu, G. D. Gu, P. D. Johnson, and U. Bovensiepen, Phys. Rev. B **89**, 115115 (2014).
[8]C. L. Smallwood, J. P. Hinton, C. Jozwiak, W. Zhang, J. D. Koralek, H. Eisaki, D.-H. Lee, J. Orenstein, and A. Lanzara, Science **336**, 1137 (2012).
[9]J. A. Sobota, S. Yang, J. G. Analytis, Y. L. Chen, I. R. Fisher, P. S. Kirchmann, and Z.-X. Shen, Phys. Rev. Lett. **108**, 117403 (2012).
[10]M. Hajlaoui, E. Papalazarou, J. Mauchain, G. Lantz, N. Moisan, D. Boschetto, Z. Jiang, I. Miotkowski, Y. P. Chen, A. Taleb-Ibrahimi, L. Perfetti, and M. Marsi, Nano Lett. **12**, 3532 (2012).
[11]A. Crepaldi, B. Ressel, F. Cilento, M. Zacchigna, C. Grazioli, H. Berger, P. Bugnon, K. Kern, M. Grioni, and F. Parmigiani, Phys. Rev. B **86**, 205133 (2012).
[12]J. A. Sobota, S.-L. Yang, A. F. Kemper, J. J. Lee, F. T. Schmitt, W. Li, R. G. Moore, J. G. Analytis, I. R. Fisher, P. S. Kirchmann, T. P. Devereaux, and Z.-X. Shen, Phys. Rev. Lett. **111**, 136802 (2013).
[13]U. Höfer, I. L. Shumay, C. Reuß, U. Thomann, W. Wallauer, and T. Fauster, Science **277**, 1480 (1997).
[14]H. Petek and S. Ogawa, Prog. Surf. Sci. **56**, 239 (1998).
[15]T. Hertel, E. Knoesel, M. Wolf, and G. Ertl, Phys. Rev. Lett. **76**, 535 (1996).
[16]U. B. P. S. Kirchmann, P. A. Loukakos, and M. Wolf, New J. Phys. **7**, 113 (2005).
[17]S. Passlack, S. Mathias, O. Andreyev, D. Mittnacht, M. Aeschlimann, and M. Bauer, J. Appl. Phys. **100**, 024912 (2006).
[18]S. Hellmann, K. Rossnagel, M. Marczynski-Bühlow, and L. Kipp, Phys. Rev. B **79**, 035402 (2009).
[19]D. Leuenberger, H. Yanagisawa, S. Roth, J. Osterwalder, and M. Hengsberger, Phys. Rev. B **84**, 125107 (2011).
[20]T. B. Norris, Opt. Lett. **17**, 1009 (1992).
[21]E. Carpene, E. Mancini, C. Dallera, G. Ghiringhelli, C. Manzoni, G. Cerullo, and S. De Silvestri, Rev. Sci. Instrum. **80**, 055101 (2009).
[22]C. L. Smallwood, C. Jozwiak, W. Zhang, and A. Lanzara, Rev. Sci. Instrum. **83**, 123904 (2012).
[23]J. Faure, J. Mauchain, E. Papalazarou, W. Yan, J. Pinon, M. Marsi, and L. Perfetti, Rev. Sci. Instrum. **83**, 043109 (2012).
[24]J. D. Koralek, J. F. Douglas, N. C. Plumb, J. D. Griffith, S. T. Cundiff, H. C. Kapteyn, M. M. Murnane, and D. S. Dessau, Rev. Sci. Instrum. **78**, 053905 (2007).
[25]P. Siffalovic, M. Drescher, M. Spieweck, T. Wiesenthal, Y. C. Lim, R. Weidner, A. Elizarov, and U. Heinzmann, Rev. Sci. Instrum. **72**, 30 (2001).
[26]S. Mathias, L. Miaja-Avila, M. M. Murnane, H. Kapteyn, M. Aeschlimann, and M. Bauer, Rev. Sci. Instrum. **78**, 083105 (2007).
[27]G. L. Dakovski, Y. Li, T. Durakiewicz, and G. Rodriguez, Rev. Sci. Instrum. **81**, 073108 (2010).
[28]P. Wernet, J. Gaudin, K. Godehusen, O. Schwarzkopf, and W. Eberhardt, Rev. Sci. Instrum. **82**, 063114 (2011).
[29]C. Schriever, S. Lochbrunner, P. Krok, and E. Riedle, Opt. Lett. **33**, 192 (2008).
[30]C. Homann, C. Schriever, P. Baum, and E. Riedle, Opt. Express **16**, 5746 (2008).
[31]M. Bradler, P. Baum, and E. Riedle, Appl. Phys. B **97**, 561 (2009).
[32]G. Cerullo and S. De Silvestri, Rev. Sci. Instrum. **74**, 1 (2003).
[33]H. Shen, S. Adachi, T. Horio, and T. Suzuki, Opt. Express **19**, 22637 (2011).
[34]M. Bradler and E. Riedle, Opt. Lett. **39**, 2588 (2014).
[35]P. Martin, S. Vivirito, and G. Petite, J. Phys. B **33**, 767 (2000).
[36]J. Mauchain, Y. Ohtsubo, M. Hajlaoui, E. Papalazarou, M. Marsi, A. Taleb-Ibrahimi, J. Faure, K. A. Kokh, O. E. Tereshchenko, S. V. Eremeev, E. V. Chulkov, and L. Perfetti, Phys. Rev. Lett. **111**, 126603 (2013).
[37]K. Ishizaka, M. S. Bahramy, H. Murakawa, M. Sakano, T. Shimojima, T. Sonobe, K. Koizumi, S. Shin, H. Miyahara, A. Kimura, K. Miyamoto, T. Okuda, H. Namatame, M. Taniguchi, R. Arita, N. Nagaosa, K. Kobayashi, Y. Murakami, R. Kumai, Y. Kaneko, Y. Onose, and Y. Tokura, Nat. Mater. **10**, 521 (2011).
[38]A. Crepaldi, L. Moreschini, G. Autès, C. Tournier-Colletta, S. Moser, N. Virk, H. Berger, P. Bugnon, Y. J. Chang, K. Kern, A. Bostwick, E. Rotenberg, O. V. Yazyev, and M. Grioni, Phys. Rev. Lett. **109**, 096803 (2012).
[39]G. Landolt, S. V. Eremeev, Y. M. Koroteev, B. Slomski, S. Muff, T. Neupert, M. Kobayashi, V. N. Strocov, T. Schmitt, Z. S. Aliev, M. B. Babanly, I. R. Amiraslanov, E. V. Chulkov, J. Osterwalder, and J. H. Dil, Phys. Rev. Lett. **109**, 116403 (2012).
[40]D. Pines and P. Nozières, *The Theory of Quantum Liquids* (Benjamin, New York, 1966).